

The spotty donor star in the X-ray transient Cen X–4

T. Shahbaz,^{1,2★†} C. A. Watson³ and V. S. Dhillon⁴

¹*Instituto de Astrofísica de Canarias (IAC), E-38200 La Laguna, Tenerife, Spain*

²*Departamento de Astrofísica, Universidad de La Laguna (ULL), E-38206 La Laguna, Tenerife, Spain*

³*Department of Physics and Astronomy, Queens University Belfast, Belfast BT7 1NN, UK*

⁴*Department of Physics and Astronomy, University of Sheffield, Sheffield S3 7RH, UK*

Accepted 2014 February 6. Received 2014 February 6; in original form 2013 October 24

ABSTRACT

We accurately determine the fundamental system parameters of the neutron star X-ray transient Cen X–4 solely using phase-resolved high-resolution UV–Visual Echelle Spectrograph spectroscopy. We first determine the radial-velocity curve of the secondary star and then model the shape of the phase-resolved absorption line profiles using an X-ray binary model. The model computes the exact rotationally broadened, phase-resolved spectrum and does not depend on assumptions about the rotation profile, limb-darkening coefficients and the effects of contamination from an accretion disc. We determine the secondary star-to-neutron star binary mass ratio to be 0.1755 ± 0.0025 , which is an order of magnitude more accurate than previous estimates. We also constrain the inclination angle to be $32^{+8}_{-2}^\circ$. Combining these values with the results of the radial-velocity study gives a neutron star mass of $1.94^{+0.37}_{-0.85} M_\odot$ consistent with previous estimates. Finally, we perform the first Roche tomography reconstruction of the secondary star in an X-ray binary. The tomogram reveals surface inhomogeneities that are due to the presence of cool starspots. A large cool polar spot, similar to that seen in Doppler images of rapidly rotating isolated stars, is present on the Northern hemisphere of the K7 secondary star and we estimate that ~ 4 per cent of the total surface area of the donor star is covered with spots. This evidence for starspots supports the idea that magnetic braking plays an important role in the evolution of low-mass X-ray binaries.

Key words: binaries: close – stars: fundamental parameters – stars: individual: Cen X–4 – stars: neutron – X-rays: binaries.

1 INTRODUCTION

In interacting binaries, such as dwarf novae and X-ray transients, the secondary star’s rotational broadening ($V_{\text{rot}} \sin i$) combined with the radial-velocity semi-amplitude (K_2) is normally used to determine the binary mass ratio of the system q ($=M_2/M_1$: where M_1 and M_2 are the mass of the compact and secondary star, respectively). However, due to the faintness of the secondary star, its rotational broadening is usually determined by using intermediate-resolution (~ 0.5 – 1.0 \AA) spectroscopy, where $V_{\text{rot}} \sin i$ is typically 30 – 100 km s^{-1} . With intermediate-resolution spectroscopy the information about the shape of the absorption lines is lost, and therefore the only information that can be extracted is the amount by which the stellar spectrum is broadened. The procedure commonly used to measure the secondary star’s rotational broadening is to

compare it to the spectrum of a slowly rotating template star, observed with the same instrumental configuration, which has been convolved with a limb-darkened standard rotation profile (Gray 1992). One assumes a limb-darkening coefficient for the spectral line and usually adopts zero limb darkening or the continuum value (which depends on the wavelength and the star’s effective temperature). The width of the standard rotation profile is varied until an optimum match is found with the target spectrum (see Marsh, Robinson & Wood 1994).

Shahbaz (1998) showed that, in principle, it is possible to use the shape of the secondary star’s absorption lines to determine the binary system parameters. In particular, one can determine the binary mass ratio directly by comparing the secondary star’s line profile with a model line profile for the Roche lobe filling secondary star’s geometry. Indeed, Shahbaz (2003) presented a model XRB-SPECTRUM, for determining the mass ratio of interacting binaries by directly fitting the observed line profile with synthetic spectra. The author makes direct use of NEXTGEN model atmosphere intensities (Hauschildt, Allard & Baron 1999), which are the most comprehensive and detailed models available for cool stars. The model fully

*E-mail: tsh@iac.es

†Based on observations collected at the European Southern Observatory, Chile, under the programme 081.D-0513(A).

takes into account the varying temperature and gravity across the secondary star’s photosphere, by incorporating the synthetic spectra into the secondary star’s Roche geometry. As a result, Shahbaz (1998) determines the exact rotationally broadened line profile of the secondary star and so eliminate the need for a limb-darkening law and the uncertainties associated with it.

X-ray transients are a subset of low-mass X-ray binaries (LMXBs) that display episodic, dramatic X-ray and optical outbursts, usually lasting for several months. Between outbursts, X-ray transients remain in a quiescent state, with typical X-ray luminosities less than 10^{32} erg s $^{-1}$, allowing the optical detection of the faint low-mass donor star. This allows the possibility to perform radial-velocity studies, probe the nature of the compact star and to also determine its mass (e.g. Charles & Coe 2006).

The neutron star X-ray transient Cen X–4 was discovered in 1969 by the *Vela 5B* satellite (Conner, Evans & Belian 1969) when it went into X-ray outburst. During its second outburst in 1979, the optical counterpart was discovered (Canizares, McClintock & Grindlay 1980) and the mass accreting star was identified as a neutron star due to the fact that it displayed a type I X-ray burst (Matsuoka et al. 1980). After 1980, Cen X–4 stayed in quiescence at $V \simeq 18.2$ and subsequent photometric studies led to the discovery of the orbital period $P_{\text{orb}} = 15.1$ h (Chevalier et al. 1989) and the determination of the companion star’s radial-velocity curve (Cowley et al. 1988; McClintock & Remillard 1990; Torres et al. 2002; D’Avanzo et al. 2005; Casares et al. 2007). Shahbaz, Naylor & Charles (1993) modelled the quiescent *H*-band light curve as due to the Roche lobe filling secondary star’s ellipsoidal modulation and obtained a binary inclination in the range $i = 31^{\circ}$ – 54° , assuming no contamination from the accretion disc. Using IR spectroscopy, Khargharia, Froning & Robinson (2010) determined the contribution of the secondary star to the infrared flux and remodelled the *H*-band light curve of Shahbaz et al. (1993), correcting for the fractional contribution of the donor star to obtain an inclination angle of $35^{\circ+4^{\circ}}_{-1^{\circ}}$.

Torres et al. (2002) obtained high-resolution optical spectroscopy of Cen X–4 and determined the mass function to be $f(M) = 0.220 \pm 0.005 M_{\odot}$, which was later refined by D’Avanzo et al. (2005) to $f(M) = 0.201 \pm 0.004 M_{\odot}$. D’Avanzo et al. (2006) searched for the effects of irradiation on the absorption-line radial-velocity curve and concluded that there is no evidence for irradiation. Casares et al. (2007) obtained much tighter constraints on $K_2 = 144.6 \pm 0.3$ km s $^{-1}$ and $P_{\text{orb}} = 0.629\ 0522 \pm 0.000\ 0004$ d and also determined $V_{\text{rot}} \sin i = 44 \pm 3$ km s $^{-1}$ and $q = 0.20 \pm 0.03$, using the standard method by comparing the observed spectrum with a template star convolved with a limb-darkened rotation profile. Estimates for the secondary star’s spectral type using optical spectroscopy include a K7 V star (Shahbaz et al. 1993) and a K3–K5 V star (Torres et al. 2002; D’Avanzo et al. 2005). González Hernández et al. (2005) determined $T_{\text{eff}} = 4500$ K and $\log g = 3.9$, corresponding to a K4 V star, as well as the chemical abundances.

The measurement of stellar masses in quiescent X-ray transients relies on the determination of K_2 and q from spectroscopy and i normally from photometry (via ellipsoidal modulation studies of the optical/IR light curves). This is mainly due to the fact that the secondary stars in quiescent X-ray transients are optically extremely faint, making it difficult for one to determine accurate masses from spectroscopy alone. In non-eclipsing systems, the main uncertainty in the mass measurements is in the determination of i . If, in the future, i can be determined to a better accuracy, then one can combine it with an accurate determination of q to measure precise binary masses. In this paper, we determine the system parameters of Cen X–4 (primarily q and i) by modelling the secondary star’s

Table 1. Log of VLT+UVES observations.

UT Date	UT range	# Spectra
2008 June 08	01:05–07:39	43
2008 June 09	02:59–04:38	12
2008 June 13	00:16–00:51	5
2008 June 23	00:00–05:06	35

Roche lobe distorted absorption-line profiles with our X-ray binary model. We also use for the first time the technique of Roche tomography to map the surface inhomogeneities on the secondary star in an LMXB.

2 OBSERVATIONS AND DATA REDUCTION

We obtained spectra of Cen X–4 in service mode during 2008 June with the UV–Visual Echelle Spectrograph (UVES) at the European Southern Observatory, Observatorio Cerro Paranal, using the 8.2 m Very Large Telescope (VLT). The UVES standard dichroic DIC1 was used yielding spectra covering the wavelength ranges 4727–5806 Å (hereafter green) and 5762–6837 Å (hereafter red). In total, 105 spectra of Cen X–4 using an exposure time of 480 s were taken as well as a spectrum of a K4 V spectral-type template star (HD 159341). A log of the observations is shown in Table 1. A 0.8 arcsec slit was used resulting in a resolving power of 50 900 and an instrumental resolution of 5.9 km s $^{-1}$ measured from the full width at half-maximum (FWHM) of the arc lines. We used the UVES pipeline software which provides an absolute flux-calibrated spectrum. The procedure consisted of bias subtraction, flat-fielding, wavelength calibration using thorium–argon lamps and absolute flux calibration. In what follows, we only use 90 red spectra (the spectra taken on June 13 were not usable), because the signal-to-noise of the green spectra was poor due to the faintness of the source in this wavelength region.

3 THE RADIAL-VELOCITY CURVE AND MEAN SPECTRUM

Spectroscopic studies of the optical counterparts in quiescent X-ray transients include the determination of the radial-velocity curve and the rotational broadening using the photospheric absorption lines arising from the companion star. It has been known for some time, especially in studies of dwarf novae and polars, that substantial heating of the secondary star shifts the effective light centre of the secondary away from the centre-of-mass of the star (Davey & Smith 1992). This results in a significant distortion of the radial-velocity curve, leading to a biased semi-amplitude and a non-circular radial-velocity curve (Shahbaz et al. 2000). D’Avanzo et al. (2006) studied in detail the possible effects of irradiation on the radial-velocity curve of Cen X–4 and concluded that there are no such effects, not surprisingly given the very low quiescent X-ray (and UV) luminosity ($L_X < 5 \times 10^{32}$ erg s $^{-1}$; Cackett et al. 2013).

To determine the radial-velocity curve of Cen X–4, we normalized the individual Cen X–4 spectra and template-star spectra by dividing by a first-order polynomial fit and then subtracting a high-order spline fit to carefully selected continuum regions. This ensures that the line strength is preserved along the spectrum, which is particularly important when the absorption lines are veiled by differing amounts over a wide wavelength range. We corrected for radial-velocity shifts by cross-correlating the individual Cen X–4 spectra with the template K4 V star (rotationally broadened by 44 km s $^{-1}$

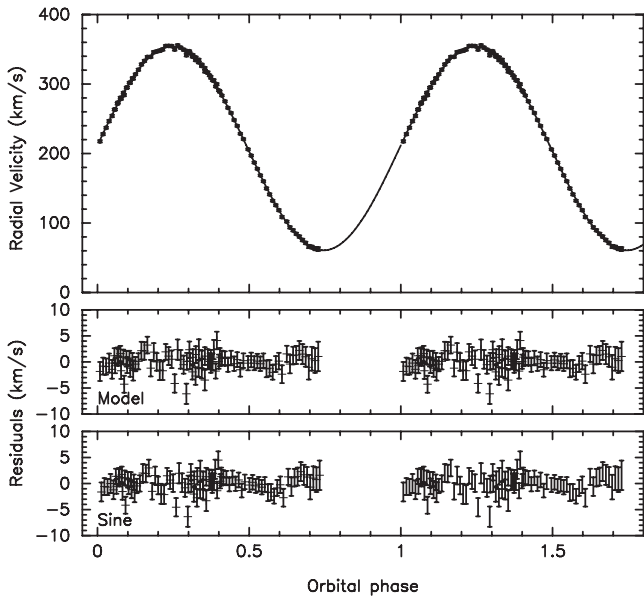


Figure 1. The heliocentric radial-velocity curve of the secondary star in Cen X-4. The solid line shows a sinusoidal fit to the data. The middle and bottom panels show the residual after subtracting an X-ray binary irradiation model and a circular orbit fit, respectively. The data have been folded on the orbital ephemeris and are shown twice for clarity.

to match the rotational velocity of the secondary star), using the method of Tonry & Davis (1979) and regions devoid of emission and interstellar lines. The radial-velocity curve, i.e. the radial velocity after correcting for the systemic radial velocity of the template star which was found to be 12.8 km s^{-1} , measured from the position of the $H\alpha$ absorption line is shown in Fig. 1.

A circular orbit fit gives the following parameters; $\gamma = 194.5 \pm 0.2 \text{ km s}^{-1}$, $K_2 = 147.3 \pm 0.3 \text{ km s}^{-1}$, $P_{\text{orb}} = 0.629\,059 \pm 0.000\,017 \text{ d}$ and $T_0 = \text{HJD } 245\,4626.6214 \pm 0.0002$, where T_0 is time at phase 0.0 defined as inferior conjunction of the secondary star and γ is the systemic velocity (1σ errors are quoted with the error bars rescaled so that the reduced χ^2 of the fit is 1.). We also fit the radial-velocity curve with our X-ray binary model (see Section 4.2), which includes the effects of irradiation. The χ^2 for the circular orbit fit and the X-ray binary model fit are 87.2 and 81.6 with 87 and 86 degrees of freedom, respectively; the residuals of the circular orbit and irradiation model fit are shown in shown in Fig. 1. An F -test concludes that the circular orbit model and the irradiation model are indistinguishable. Therefore, like D’Avanzo et al. (2006), we also conclude that there are no effects of irradiation on the absorption lines in Cen X-4.

The velocity-corrected spectra (using the circular orbit fit) were then combined to produce a variance-weighted Doppler-averaged spectrum. The Doppler-averaged spectrum of Cen X-4 and the template-star spectra were then binned on to the same uniform velocity scale ($1.6 \text{ km s}^{-1} \text{ pixel}^{-1}$). The final spectrum of Cen X-4 has a signal-to-noise ratio of ~ 45 per pixel in the continuum and is shown in Fig. 2.

4 THE BINARY MASS RATIO AND INCLINATION ANGLE

To determine the fundamental binary parameters, one would ideally like to observe a time series of high signal-to-noise unblended absorption lines at high spectral resolution. The least-squares decon-

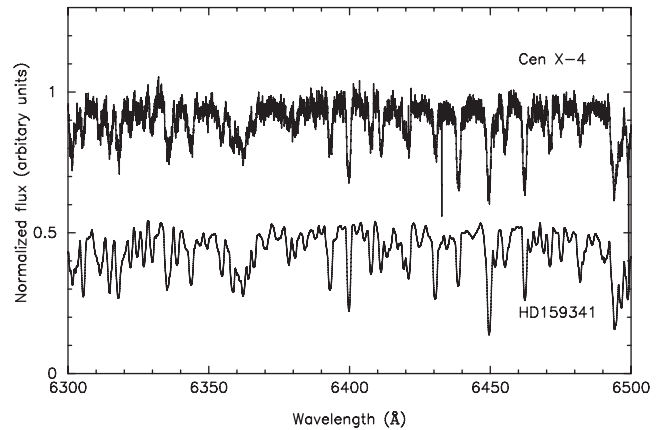


Figure 2. The Doppler-averaged spectrum of Cen X-4 (top) and the K4 V template star HD 159341 (bottom) rotationally broadened by 44 km s^{-1} .

volution (LSD) method (Donati & Collier Cameron 1997) allows us to do exactly this, since it effectively stacks the thousands of stellar absorption lines in an echelle spectrum to produce a single ‘average’ absorption-line profile with increased signal-to-noise ratio; theoretically, the increase in signal-to-noise ratio is the square root of the number of lines observed. It has been used in the spectropolarimetric observations of active stars (e.g. Donati et al. 1997) and in Doppler imaging studies (e.g. Barnes, James & Collier Cameron 2004). LSD has also been used in conjunction with Roche tomography to map the surface brightness distribution of the secondary stars in cataclysmic variables (CVs; see Watson et al. 2007 and references within) and to compute high-quality line profiles of X-ray binaries (Shahbaz 2003; Shahbaz & Watson 2007).

LSD assumes that all of the absorption lines are rotationally broadened by the same amount, and hence just requires the position and strength of the observed lines in the echelle spectrum to be known. We generated a line list appropriate for a K4 V star ($T_{\text{eff}} = 4500 \text{ K}$, $\log g = 4.0$) from the Vienna Atomic Line Database (VALD; Kupka et al. 2000). Approximately 5500 lines were used in the deconvolution process. Our version of LSD propagates the errors through the deconvolution process (for details, see Watson et al. 2007).

LSD profiles were constructed for each of the individual Doppler-corrected Cen X-4 spectra using regions devoid of emission lines and interstellar lines. We also computed the LSD profile for the K4 V template star (HD 159341). In the next sections, q is determined using two different methods. The first method uses the standard determination of $V_{\text{rot}} \sin i$ that, when combined with K_2 , gives q . The second method involves the determination of q directly using a Roche lobe filling star model.

4.1 Spherical rotation profile

The secondary stars in X-ray binaries are tidally locked and in synchronous rotation; therefore, for a given orbital period, the width of the line profile scales with the size of the star’s Roche lobe. It is easy to show that $V_{\text{rot}} \sin i$ and R_2 (the radius of a sphere whose volume is the same as the volume of the secondary star) are related through the expression

$$V_{\text{rot}} \sin i / K_2 = (1 + q) R_2 / a, \quad (1)$$

where a is the binary separation (Horne, Wade & Szkody 1986). Thus, by measuring $V_{\text{rot}} \sin i$ and K_2 , one can determine q . Previous models for the spectra of Roche lobe filling secondary stars

assume that the rotational broadening of their spectra can be modelled by convolving the spectrum of a non-rotating star with a line-broadening function for a slowly rotating spherical star, e.g. the Gray function. However, the use of the Gray profile to describe the spectra of Roche lobe filling stars produces significantly biased measurements of the rotational velocities in interacting binaries. Convolution also gives biased rotational velocities even for rapidly rotating single stars (Collins & Truax 1995). Using equation (1) to convert from rotational velocity to mass ratio leads to a 5 per cent systematic underestimate in the mass ratio when using the relations from Paczyński (1971) or Eggleton (1983) for R_2/a because they assume a spherical secondary star (Marsh et al. 1994; Welsh, Horne & Gomer 1995). The unknown limb-darkening coefficient in the line when applying the Gray broadening profile to measure $V_{\text{rot}} \sin i$ also introduces a systematic bias as large as 14 per cent. This is because of the uncertainty about the non-spherical secondary star's radius and the fact that the projected radius and hence rotational broadening and q are strongly dependent on orbital phase ϕ (Welsh et al. 1995). Thus, the correct expression for $V_{\text{rot}} \sin i$ should be

$$V_{\text{rot}}(\phi) \sin i / K_2 = (1 + q) R_2(\phi) / a \quad (2)$$

and, as pointed by Welsh et al. (1995), the spherical approximation can still be used provided that one models the phase-resolved spectra and not the mean spectrum.

To determine $V_{\text{rot}} \sin i$, the phase-resolved LSD profiles of Cen X-4 were compared to a rotationally broadened version of the template-star LSD profile using the standard optimal subtraction procedure (Marsh et al. 1994). We optimally subtracted a constant (representing the fraction of light from the template star f) multiplied by a rotationally broadened version of the template star, using a spherical rotation profile (Gray 1992) with a linear limb-darkening coefficient ($u = 0.72$; Claret 2000) appropriate for a K4 V star at the central wavelength of the red spectra. The optimal subtraction was performed over the line profile from -100 to 100 km s^{-1} . The χ^2 of the fit was calculated and the optimal rotational broadening and factor f were determined for each orbital phase. The LSD spectrum of Cen X-4 at phase 0.0 and the rotationally-broadened template-star fit is shown in Fig. 3; the χ^2 of the fit is 136.7 (132 degrees of freedom). The values determined for $V_{\text{rot}} \sin i$ and f are shown in Fig. 4, where the 1σ errors have been rescaled so that the reduced χ^2 of the fit is 1.

A Roche lobe filling star should show variations in $V_{\text{rot}} \sin i$ with orbital phase as the secondary star rotates, in a similar manner to the ellipsoidal variations (due to the star's changing projected area), which show a double-humped modulation on half the orbital period. A fit to the phase-resolved rotational velocities with a sinusoidal modulation with half the orbital period gives a mean rotational velocity of $V_{\text{rot}} \sin i = 44.9 \text{ km s}^{-1}$ with a semi-amplitude of $2.9 \pm 0.3 \text{ km s}^{-1}$. It should be noted that the analysis above assumes that the limb-darkening coefficient appropriate for the radiation in the lines is the same as for the continuum. However, in reality this is not the case, and the absorption lines in late-type stars will have core limb-darkening coefficients much smaller than that appropriate for the continuum (Collins & Truax 1995). Therefore, we also perform the analysis using zero limb darkening and obtain a similar rotational velocity modulation but with a mean $V_{\text{rot}} \sin i = 41.0 \text{ km s}^{-1}$ and a semi-amplitude of $2.9 \pm 0.3 \text{ km s}^{-1}$. Using the peak-to-peak values obtained using continuum and zero limb darkening, we obtain a $V_{\text{rot}} \sin i$ range of $38.1 (= 41.0 - 2.9)$ to $47.8 (= 44.9 + 2.9) \text{ km s}^{-1}$, which when combined with K_2 in equation (1) gives q in the range $0.139 - 0.234$. Note that our determination of q here takes into account the phase-dependent values of $V_{\text{rot}} \sin i$ and the un-

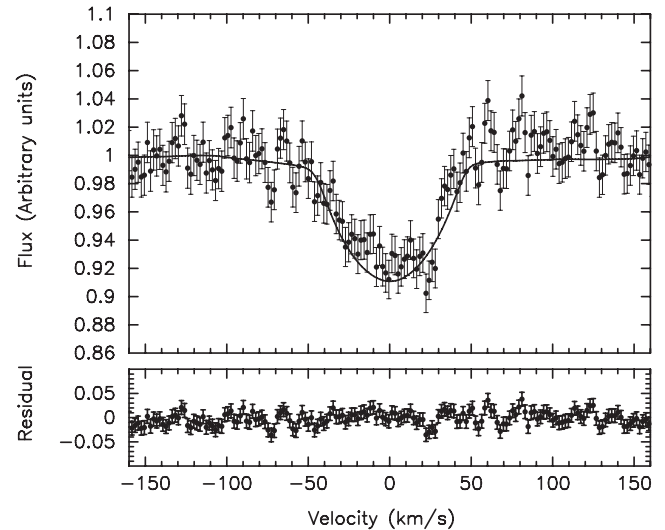


Figure 3. The determination of $V_{\text{rot}} \sin i$ for an LSD profile of Cen X-4 at orbital phase 0.0 using the standard method (see Section 4.1), where one compares the observed spectrum with a template star convolved with a limb-darkened Gray rotation profile. The solid line shows the LSD profile of the K4 V template star rotationally broadened by 44.5 km s^{-1} using a limb-darkened spherical rotation profile scaled to match the Cen X-4 LSD profile. The bottom panel shows the residual of the fit after the optimal subtraction.

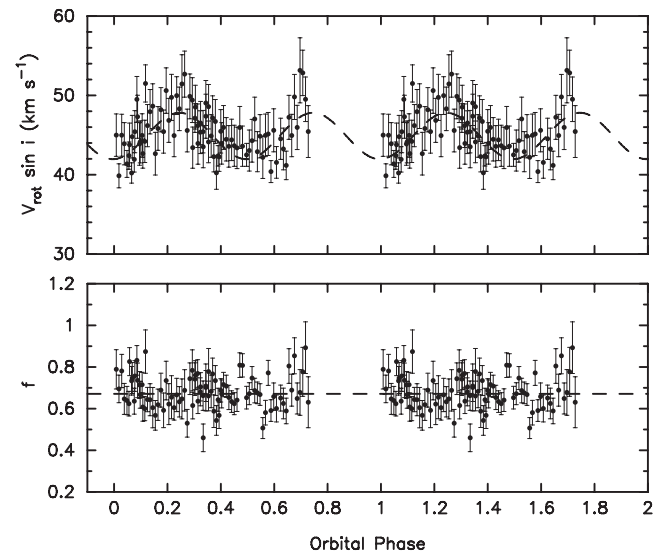


Figure 4. The results of the phase-resolved measurements of $V_{\text{rot}} \sin i$ (top panel) and f (bottom panel) in Cen X-4 determined using the LSD profiles of Cen X-4 and the standard method, where one compares the observed spectrum with a template star convolved with a limb-darkened standard Gray rotation profile. The data are shown twice for clarity.

certain line limb darkening. Casares et al. (2007) and Torres et al. (2002) obtained q values which are consistent with ours using the mean spectrum, though it should be noted that they did not take into account the phase-dependent values of $V_{\text{rot}} \sin i$.

The fractional contribution of the secondary star should mimic the ellipsoidal variations. We do not, however, find any obvious sinusoidal modulation in the fractional contribution. This may be due to short-term flaring events dominating changes in the veiling factor of the absorption lines – it is well known that such flaring events are present in all quiescent X-ray transients (Zurita, Casares

& Shahbaz 2003) as well as in Cen X–4 (Chevalier et al. 1989; Shahbaz et al. 2010). These flares are present at different levels during the different quiescent states (see Section 7.1).

4.2 Roche lobe rotation profile

In order to obtain an accurate determination of q that does not depend on assumptions about the rotation profile and limb-darkening coefficients, we use the model `XRBSPECTRUM` described in Shahbaz (2003). The model computes the exact rotationally broadened model spectrum, which can then be directly compared with the observed spectrum of Cen X–4. The parameters that determine the Roche geometry of the secondary star in an interacting binary are q , i , K_2 , T_{eff} , the Roche lobe filling factor and the gravity-darkening coefficient. We assume that the secondary fills its Roche lobe, a safe assumption in X-ray binaries given that we observed an accretion disc (Chevalier et al. 1989; Shahbaz et al. 1996). The width of the lines are primarily determined by q and K_2 , whereas i and β (the gravity-darkening coefficient) mainly determine the shape of the absorption line. The gravity-darkening coefficient was assumed to be 0.08, which is appropriate for late-type stars with a convective envelope (Lucy 1967; Sarna 1989). The velocity, gravity and temperature for each element vary across the star due to the shape of the Roche lobe. For each visible element, the model computes the local effective temperature, gravity and limb angle and then determines the specific intensity using the `NEXTGEN` model atmosphere intensities (Hauschildt et al. 1999). For a specified wavelength (limited to the range 6300–6800 Å), the model then integrates the visible specific intensity values over the visible surface of the Roche lobe and gives the exact rotationally broadened spectrum of the secondary star at a given orbital phase. The intrinsic profile has a FWHM of 9.5 km s^{-1} , which is set by the velocity scale of the `NEXTGEN` model atmospheres ($4.7 \text{ km s}^{-1} \text{ pixel}^{-1}$). The model is similar to the program `LINBROD` which uses `ATLAS9` and `MOOG` for its atmosphere and spectrum synthesis (Bitner & Robinson 2006).

In order to compare the model spectrum with the observed spectrum, we computed the model spectrum at the same orbital phases and taking into account all sources that can velocity broaden the spectra. The spectra of Cen X–4 consists of 90 Doppler-corrected spectra covering orbital phases 0.00–0.73 with exposure times of 480 s. We first computed the model spectrum for a given value of q , i , K_2 , T_{eff} and orbital phase. We then allowed for the smearing of the absorption lines due to the motion of the secondary star during the length of each exposure at each orbital phase, by convolving the model spectrum with a rectangular function. We also convolved the spectrum with a Gaussian function with FWHM equal to the instrumental resolution of the data. We also convolved the observed LSD profiles with the intrinsic line profile shape of the `XRBSPECTRUM` model spectra so that we can compare the model and observed LSD profiles, taking into account all sources of velocity broadening. Finally, given the poorer velocity dispersion of the model spectra ($4.7 \text{ km s}^{-1} \text{ pixel}^{-1}$) compared to the observed spectra ($1.6 \text{ km s}^{-1} \text{ pixel}^{-1}$), all the data and models were binned on to the same uniform velocity scale of $4.7 \text{ km s}^{-1} \text{ pixel}^{-1}$.

The model spectra were then normalized using a continuum spline fit and then LSD profiles were determined in the wavelength range 6300–6500 Å (note that we are limited in wavelength by the model synthetic spectra). We then compared each phase-resolved model LSD line profile to each observed LSD line profile by optimally subtracting a scaled version of the line profile from the observed line profile (to allow for any variable disc contribution) and computing the χ^2 of the fit. This optimal subtraction was per-

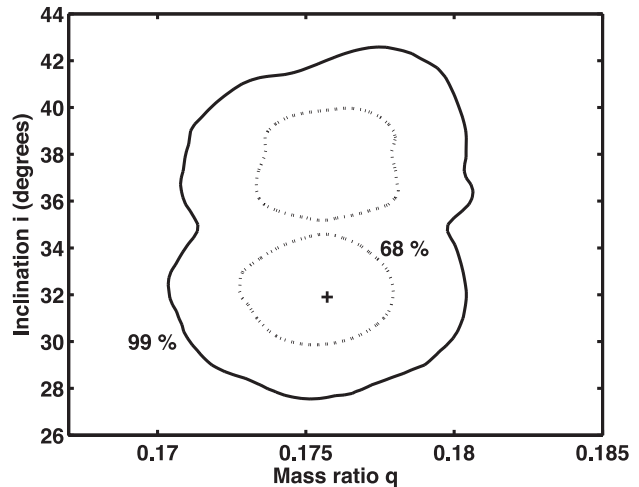


Figure 5. The result of the model LSD profile fits to the phase-resolved LSD profiles of Cen X–4 in the $(q-i)$ plane. The best fit at $q = 0.1755$ and $i = 32^\circ$ is shown with a cross and the 68 and 99 per cent confidence regions are shown as the dotted and solid lines, respectively.

formed over the line profile from -100 to 100 km s^{-1} . We then summed the χ^2 values obtained for all orbital phases.

Computing the models is computationally expensive (taking ~ 2 h of CPU time for a given q , i and orbital phase) and so we perform a preliminary grid search in the $(q-i)$ plane; q in the range 0.16–0.20 in steps of 0.01 and i in the range 30° – 50° in steps of 2.5° . A gravity-darkening coefficient of 0.08 was used throughout, the same as that has been used by previous authors to fit the optical/infrared light curves (Khargharia et al. 2010) and T_{eff} and K_2 were fixed at 4500 K (González Hernández et al. 2005) and 147.3 km s^{-1} (see Section 3), respectively. Once a minimum χ^2 was found, we increased the resolution of the grid to 0.002 and 1° in q and i , respectively. The best fit resulted in a minimum χ^2 of 3800 (3780 degrees of freedom) at $q = 0.1755$ and $i = 32^\circ$; 68 and 99 per cent confidence levels are shown in Fig. 5 (the contours have been rescaled so that the reduced χ^2 of the fit is 1). As one can see, q is well constrained to within 0.0025, whereas i is only constrained to $^{+8^\circ}_{-2^\circ}$ (68 per cent uncertainties). In Fig. 6, we show the individual LSD profiles of Cen X–4 with the best-fitting model profiles. As one can see, the model fits the data reasonably well at most orbital phases.

5 THE BINARY MASSES

Using our determined values for P_{orb} , K_2 , q and i , we can determine the binary masses using the mass function $P_{\text{orb}} K_2^3 / 2\pi G = M_1 \sin^3 i / (1+q)^2$. In order to determine the uncertainties in M_1 and M_2 , we used a Monte Carlo simulation, in which random values for the observed quantities were drawn that follow a Gaussian distribution, with mean and variance the same as the observed values. For parameters with symmetric uncertainties P_{orb} , K_2 (see Section 3), we assume the distribution to be Gaussian. We use the (q, i) solutions found in Section 4.2 to determine the actual distribution for q numerically by calculating the maximum likelihood distribution using the actual χ^2 values, for a given value of i . We then determine the cumulative probability distribution of the asymmetric distribution numerically and then pick random values for the probability to obtain random values for the parameter. We obtain $M_1 = 1.94^{+0.37}_{-0.85} M_\odot$ and $M_2 = 0.34^{+0.07}_{-0.15} M_\odot$, consistent with previous measurements (Shahbaz et al. 1993; Torres et al. 2002; Casares et al. 2007; Khargharia et al. 2010). Given the measured

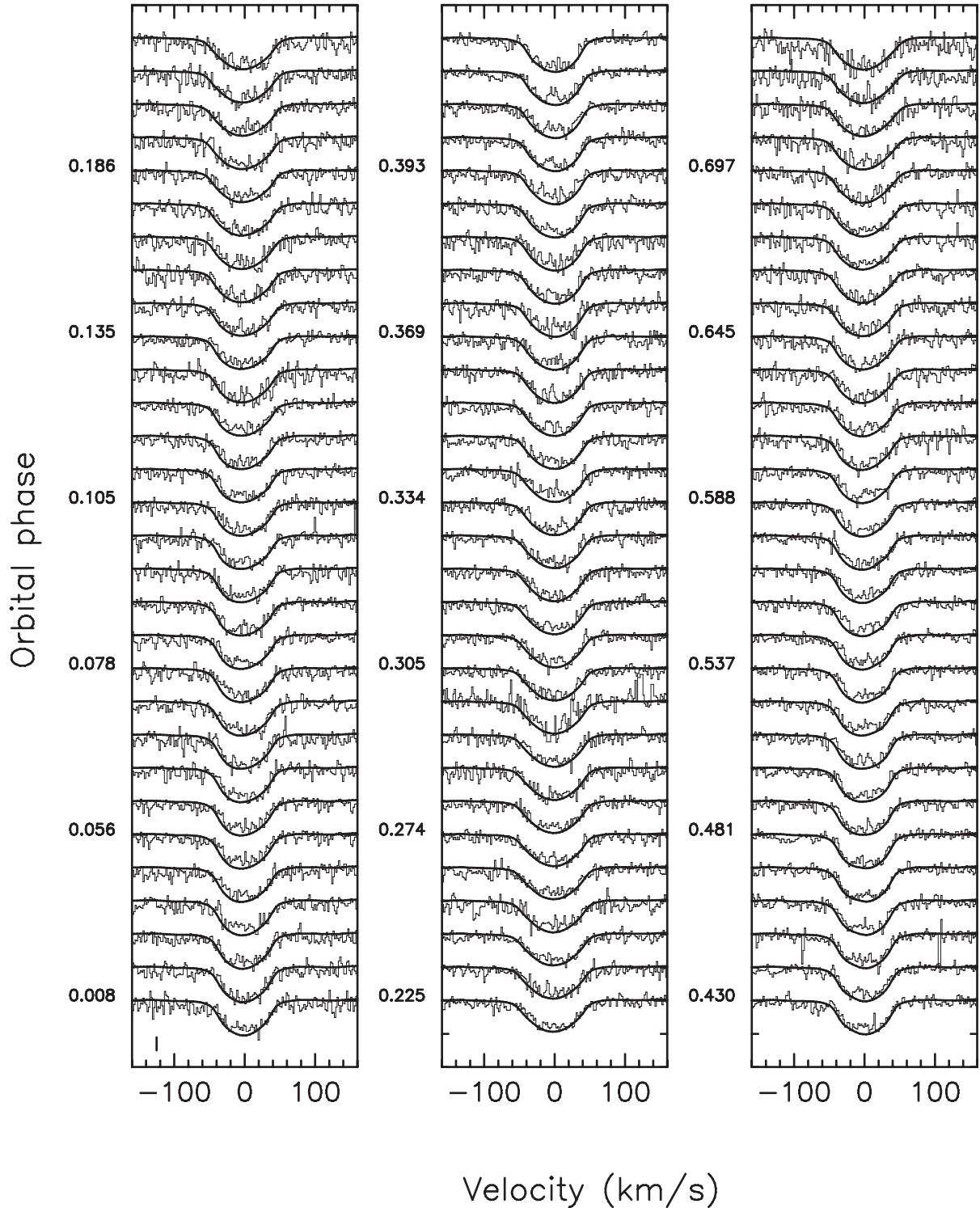


Figure 6. The best-fitting model LSD profiles (thick line) with the observed LSD profiles of Cen X-4 (thin lines). The orbital motion has been removed assuming the binary parameters found in Section 3 and the data have been shifted vertically by 0.1 (continuum units) for clarity. The typical uncertainty ($\pm 1\sigma$) in the data is shown in the bottom-left corner.

masses and orbital period, we use Kepler’s Third Law to determine a . Eggleton’s expression for the effective radius of the Roche lobe (Eggleton 1983) then determines R_2 , which with $T_{\text{eff}} = 4500$ K inferred from the spectral type (Gray 1992) and Stefan–Boltzmann’s law gives the star’s luminosity L_2 . We obtain $R_2 = 0.99^{+0.06}_{-0.18} R_{\odot}$, $L_2 = 0.36^{+0.04}_{-0.12} L_{\odot}$ and $a = 4.07^{+0.24}_{-0.72} R_{\odot}$.

6 EVIDENCE FOR STARSPOTS

It is well known that non-uniform intensity distributions on the donor star surface can introduce systematic errors in the determined binary parameters due to the fact that the centre-of-mass and the centre-of-light of the donor may no longer be coincident. So we

explored the data set for the signatures of stellar activity, such as starspots.

Roche tomography is an astrotomographic technique that images the surface of the secondary star in interacting binaries (Rutten & Dhillon 1994; Watson 2002). The procedure is fully tested and artefacts caused by systematic errors are well characterized and understood. For a detailed review of the technique, see Watson & Dhillon (2001, 2004) and Dhillon & Watson (2001). In summary, Roche tomography uses phase-resolved spectral-line profiles to produce a map of the line-intensity distribution across the secondary star's surface in three-dimensional real space. It is analogous to Doppler imaging of single stars, but with the difference that the star is assumed to be Roche lobe filling, rotates around the binary centre-of-mass, is tidally locked and has undergone orbital circularization.

While Doppler tomography (Marsh & Horne 1988) is a frequently used tool for mapping the components in CVs and X-ray binaries in velocity space, Roche tomography has the advantage that it can deal with effects such as self-obscurance and limb darkening of the donor star and is better suited to studies of the stellar components in such systems. When performing Roche tomography, it is important to use the correct system parameters (i , q , M_1 and M_2), as if incorrect system parameters are adopted, then these will introduce spurious artefacts in the final tomogram (Watson & Dhillon 2001). The system parameters are normally obtained by constructing *entropy landscapes*, where reconstructions to the same χ^2 are carried out for different combinations of component masses, and the entropy obtained in the final map for each pairing is plotted on a grid of M_1 versus M_2 . Since entropy encodes the information content in the map and adopting incorrect system parameters introduces spurious artefacts in the reconstruction, the parameters that yield the map with the least information content and therefore least structure (maximum entropy) due to artefacts are selected.

We constructed a series of entropy landscapes (see Watson et al. 2007 and references therein for a detailed description of the technique) for various orbital inclinations in order to provide an independent estimate of the system parameters. Since Roche tomography treats limb darkening in a different manner to the XRBSPECTRUM model analysis outlined in Section 4.2, this was carried out for the case of no limb darkening and also assuming a square root limb-darkening law with coefficients of $c = 0.522$ and $d = 0.362$ (consistent with the tabulated values from Claret 1998 for a star with $T_{\text{eff}} = 4500$ K and $\log g = 4.0$ centred on the R band). Our initial results gave mass ratios of $q = 0.197 \pm 0.011$ in the case of no limb darkening and significantly higher mass ratios when limb darkening was assumed – inconsistent with that found in the XRBSPECTRUM analysis ($q = 0.1755 \pm 0.0025$). This discrepancy was tracked down to a combination of the relatively low signal-to-noise of the data set for Roche tomography purposes, coupled with a systematic noise bias in the continuum introduced by the technique. In detail, the maximum-entropy algorithm that is implemented in Roche tomography requires that all data are positive. For absorption lines, this means that the profile is first inverted and then all remaining negative data points are set to zero. This results in a positive ‘biasing’ of the noise in the continuum regions, and for low signal-to-noise data an improved fit can be found by artificially inflating the Roche lobe so that the positive noise near the line-wings can be fitted as well – leading to a systematically higher value for q . In order to surmount this problem, we have added a ‘virtual pixel’ to the reconstruction process that contributes a constant value to all velocity bins at all phases. This injects an offset to the data that is then fitted within the image reconstruction process, with the result that the initially

negative data points no longer need to be cropped. The addition of a virtual pixel has previously been implemented for low signal-to-noise data in Roche tomography by Watson et al. (2003), where we found a similar impact on the determination of the component masses.

After implementing this correction, we found that while we were unable to reliably constrain the inclination, the mass ratios found at $i = 32^\circ$ bracketed those determined by the XRBSPECTRUM analysis ($q = 0.1755 \pm 0.0025$). In the case of no limb darkening, we find $q = 0.168$, whereas for the root limb-darkening case, we find $q = 0.195$. We suspect that the better treatment of limb darkening by XRBSPECTRUM leads to a better binary parameter constraint in this case. For low signal-to-noise data, Roche tomography may additionally be biased as it attempts to fit features due to noise – something that XRBSPECTRUM is less prone to.

In Fig. 7, we show the results of the Roche tomography reconstruction of the secondary star in Cen X–4 using the LSD profiles. The data and corresponding fit are displayed as well as the residuals. To allow the reader to see the spot features more clearly, we also show the residuals after a theoretical line-profile assuming a blank unspotted stellar surface is subtracted from each LSD profile in order to enhance starspot features. The Roche tomogram is shown in Fig. 8. The most notable feature in the Roche tomogram is a large, dark starspot feature which lies in the Northern polar region; the dark region at the inner Lagrangian point is due to gravity darkening, as expected for a Roche lobe filling star (Shahbaz 1998). This can also be seen in the trailed spectra as a feature that runs through the spectra remaining near the core of the lines and is visible throughout the orbital cycle (as expected for a high-latitude feature seen on a star with a relatively low inclination angle).

While the Roche tomogram shows a number of features, such as small-scale dark regions and streaks at all latitudes, the majority of these are due to the projection of noise in the data set. Indeed, the spectra are only just of sufficiently high signal-to-noise to confidently recover large features that have high visibility (such as the polar-spot feature). We are, however, confident in the detection of the polar spot as it is both visible in the trailed spectra and also covers a far larger surface area than can be attributed to noise (which creates artefacts on a much smaller scale). Calculating robust parameters for the polar spot, such as its filling-factor and area, is made difficult due to the low signal-to-noise of the data set relative to that obtained in other spot maps of CV donors reconstructed with Roche tomography (Watson et al. 2003, 2007; Watson, Dhillon & Shahbaz 2006). Therefore, we have only attempted to calculate an approximate spot coverage of the polar feature – which we find covers ~ 4 per cent of the total surface area of the donor star. The true polar-spot coverage is likely to be higher, since only the most prominent (darkest) spots can be confidently detected in this data set and regions of lower spot-filling factors will be difficult to discern. Nonetheless, this is an appreciable size and indicates that LMXB donor stars, like in CVs, also have high global spot coverages (Watson et al. 2007). This Roche tomogram therefore represents the first concrete observational evidence of strong magnetic activity on the donor stars in LMXBs.

To see if the polar spot affected our determination of q and i in Section 4.2, we used our XRBSPECTRUM model to simulate spectra with a polar spot (10 per cent in area) for given q and i ; we set regions on the star grid near the pole to an effective temperature 1000 K lower than the immaculate, unspotted photosphere. We also added instrumental broadening and finally orbital smearing, matching that of the observed data. We then produced LSD profiles before finally performing a grid search in q and i using our XRBSPECTRUM model

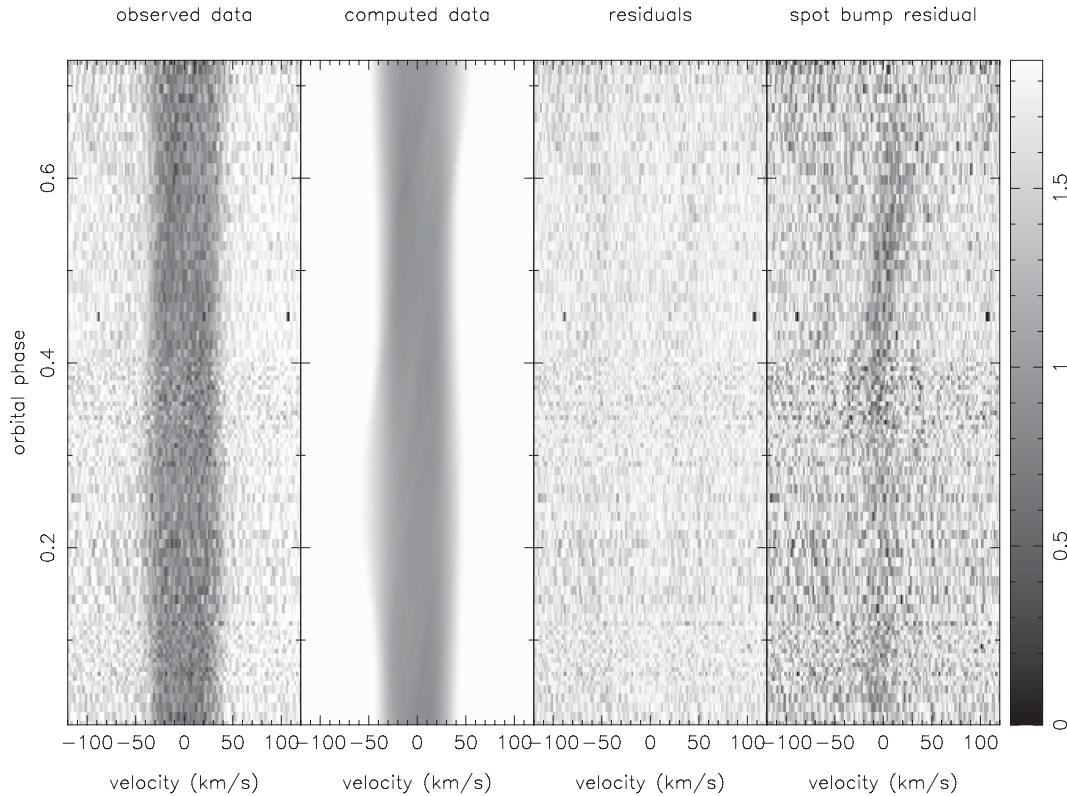


Figure 7. Triled spectra of Cen X-4 showing (from left to right), the observed LSD data, computed data from the Roche tomography reconstruction and the residuals. Starspot features in these three panels appear bright. A grey-scale intensity wedge is also shown, where a value of 1 corresponds to the maximum line depth in the reconstructed profiles. In the final (right-hand) panel, we plot the residuals after a theoretical line-profile assuming an unspotted stellar surface was subtracted from each LSD profile in order to enhance starspot features. In this case, spot features now appear dark in the plots and the contrast has been stretched by a factor of 1.5 to further enhance the spot features. The orbital motion has been removed assuming the binary parameters found in Sections 3 and 4.2, which allows the individual starspot tracks across the profiles and the variation in $V_{\text{rot}} \sin i$ to be more clearly observed.

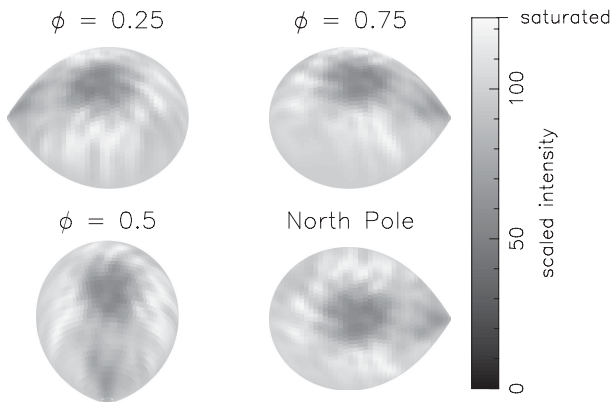


Figure 8. Roche tomogram of Cen X-4. The intensity scale is such that dark scales represent regions of lower absorption and as such both starspots and any region of ionizing irradiation would both appear dark. The map is shown as the observer would see it at an inclination of $i = 32^\circ$ except for the lower-right image, where the observer is directly above the North pole.

to fit the data. We find that we recover the q and i values of our simulated data. This is not surprising because a polar spot viewed on a system with a low inclination angle will be observable at all orbital phases, and it will predominantly only affect the core of the line profiles. The determination of q and i using our XRBSPECTRUM model, on the other hand, depends heavily on the *asymmetry* of the

line profiles, and is therefore not greatly affected by features present in the core of the lines (see Section 7.1).

7 DISCUSSION

7.1 The determination of q and i

Shahbaz et al. (1993) modelled the quiescent H -band light curve of Cen X-4 as due to the Roche lobe filling secondary star's ellipsoidal modulation and obtained i in the range 31° – 54° , assuming no contamination from the accretion disc. Using IR spectroscopy, Khargharia et al. (2010) determined the contribution of the secondary star to the infrared flux. They then remodelled the H -band light curve of Shahbaz et al. (1993), correcting for the fractional contribution of the donor star to obtain an inclination angle of $35^\circ_{-1^\circ}^{+4^\circ}$. However, as noted by these authors, there are a number of systematic effects that may not be accounted for in their uncertainties on i . Mismatches between template and donor star in temperature, gravity or metallicity would lead to an uncertain determination of the secondary star's contribution to the infrared flux. Also it is known that the shape and amplitude of the light curve is not consistent throughout quiescence, there are various different states characterized by magnitude, colour and aperiodic variability (Cantrell et al. 2008, 2010). Determining the contribution of the secondary star requires contemporaneous light curves and spectroscopy. The presence of starspots introduce systematic errors in the determination of i obtained by modelling optical/infrared light curves. Gelino,

Harrison & Orosz (2001) observed anomalies in the infrared continuum light curve of A 0620–00, which they modelled as cool starspots on the secondary star. They found that starspots affect the derived inclination angle by $\sim 1^\circ$. In Cen X–4, there is no evidence for starspots in the light curves, but this could be due to the fact that the light curves are dominated by aperiodic variability (Chevalier et al. 1989; Shahbaz et al. 2010). Also, if the dominant spot is located over the polar regions, as seen in the Roche tomograms presented in this paper, then there will be little rotational modulation due to the spot as it is always in view.

Shahbaz (1998) assessed the effects of the physical processes that determine the shape of the absorption lines in the spectra of Roche lobe filling stars. They found that i primarily affects the degree of asymmetry of the line profiles near orbital phases 0.0–0.1 and 0.4–0.5 and not the actual widths. The lines become more asymmetric as i increases and $\sim 40^\circ$ seems to mark the angle where the asymmetry of the line profiles are zero. Our determination of q and i does not depend on the depth of the absorption lines and only depends on the shape of the phase-dependent line profiles. Starspots present near the stellar limb will result in line profiles that appear narrower, whereas starspots present near the disc centre and/or at high latitudes/poles will result in flat-bottomed line profiles which only affect the core of the line profiles. For a low-inclination system like Cen X–4, a polar spot is observed at all orbital phases and so will have a similar effect on all the phase-resolved line profiles, and given that it does not affect the line wings, the polar spot does not affect the determination of q and i (see Section 4.2). Our determination of q is accurate to 1.4 per cent because we model the exact shape of the rotationally broadened line profiles in a way that does not depend on assumptions about the rotation profile, limb-darkening coefficients and the effects of contamination from an accretion disc. Previous estimates for q are only accurate to 15 per cent (Casares et al. 2007) mainly because of the uncertainties in the limb-darkening coefficient and our determination is a factor of ~ 10 more accurate. Our determination of i is accurate to 5° , similar to that found by previous authors (Khargharia et al. 2010), but it should be noted that our determination is not affected by aperiodic variability or polar starspots.

7.2 The implications of starspots

Rotating single stars cooler than about 6500 K with spectral types later than F5 have convective outer layers. They create a dynamo that amplifies the internal magnetic fields and brings them to the stellar surface. Angular momentum is then removed from the stellar surface by the action of the magnetically coupled stellar wind, the mechanism being called ‘magnetic braking’ (Schatzman 1962). The low-mass secondary stars in CVs and LMXBs should also have magnetic fields since they also have deep convection zones and are rapidly rotating since they are tidally locked with their compact companion star. Therefore, magnetic braking is thought to be the fundamental mechanism responsible for orbital angular momentum loss in CVs and LMXBs, which maintains the mass transfer from the low-mass donor to the more massive compact companion (Verbunt & Zwaan 1981; Rappaport, Verbunt & Joss 1983). Indeed, magnetic braking is crucial in the standard explanation for the deficit of CVs with orbital periods between 2 and 3 h (the ‘period gap’; Robinson et al. 1981; Rappaport et al. 1983; Spruit & Ritter 1983).

The secular evolution of LMXBs follows two paths, depending on the evolutionary stage of the companion star at the start of the mass transfer. Pylyser & Savonijje (1988) found that there is a bifurcation period at ~ 12 h for the initial binary orbital period

which separates converging and diverging binaries. More recent works suggest a bifurcation of 0.5–1 d; however, its precise value depends on the treatment of tidal interactions and magnetic braking (e.g. van der Sluys, Verbunt & Pols 2005; Ma & Li 2009) and is still a subject of debate. If the orbital period at the beginning of the mass transfer is above the bifurcation period, the evolution of the binary begins when the companion evolves off the main sequence, the mass transfer is driven by the internal evolution of the low-mass (sub)giant companion star and the system will evolve towards large orbital periods. If the orbital period of the system at the onset of the mass transfer is below the bifurcation period, the companion star is relatively unevolved, and the only important mechanism driving mass transfer is systemic angular momentum loss due to magnetic braking and gravitational radiation, which eventually leads to stripped, evolved companion stars. For angular momentum loss due to magnetic braking, the secondary star must have a convective envelope (Rappaport et al. 1983), which implies that the initial mass of the secondary star has to be less than $1.5 M_\odot$ (stars above this mass have radiative envelopes). Our evidence for a polar spot on the secondary star in Cen X–4 (see Section 6) implies that the star must have a convective envelope and thus supports the idea that magnetic braking plays an important role in the evolution of LMXBs.

8 CONCLUSIONS

We have determined the system parameters of the X-ray transient Cen X–4 using only phase-resolved high-resolution UVES spectroscopy. We first determined the radial-velocity curve of the secondary star. We then modelled the shape of the phase-resolved absorption line profiles using our X-ray binary model XRBSPCTRM that computes the exact rotationally broadened phase-resolved spectrum. This approach does not depend on any assumptions regarding the shape of the rotation profile, limb-darkening coefficients or laws, or the effects of contamination from an accretion disc. We determined the binary mass ratio of 0.1755 ± 0.0025 which is a factor of ~ 10 more accurate than previous estimates. We also constrain the inclination angle to $32^\circ_{-2^\circ}^{+8^\circ}$. Combining these values with the results of the radial-velocity study gives a neutron star mass of $1.94_{-0.85}^{+0.37} M_\odot$, consistent with previous estimates.

We present the first Roche tomography reconstruction of the secondary star in an LMXB, which reveals the presence of a large, cool polar starspot, similar to those seen in Doppler images of rapidly rotating isolated stars. The detection of a starspot supports the idea that magnetic braking plays an important role in the evolution of LMXBs.

ACKNOWLEDGEMENTS

We would like to thank Tom Marsh for the use of his MOLLY software package. We acknowledge the use of the VALD for obtaining our atomic line lists. This paper makes use of the IAC’s Supercomputing facility CONDOR. This research has been supported by the Spanish Ministry of Economy and Competitiveness (MINECO) under the grant (project reference AYA2010-18080). CAW and VSD are supported by the STFC.

REFERENCES

- Barnes J. R., James D. J., Collier Cameron A., 2004, MNRAS, 352, 589
 Bitner M. A., Robinson E. L., 2006, AJ, 131, 1712

- Cackett E. M., Brown E. F., Degenaar N., Miller J. M., Reynolds M., Wijnands R., 2013, *MNRAS*, 433, 1362
- Canizares C. R., McClintock J. E., Grindlay J. E., 1980, *ApJ*, 236, L55
- Cantrell A. G., Bailyn C. D., McClintock J. E., Orosz J. A., 2008, *ApJ*, 673, L159
- Cantrell A. G. et al., 2010, *ApJ*, 710, 1127
- Casares J., Bonifacio P., González Hernández J. I., Molaro P., Zoccali M., 2007, *A&A*, 470, 1033
- Charles P. A., Coe M. J., 2006, in Lewin W., van der Klis M., eds, *Compact Stellar X-ray Sources*. Cambridge Astrophys. Ser., No. 39, Compact Stellar X-ray Sources. Cambridge Univ. Press, Cambridge, p. 215
- Chevalier C., Ilovaisky S. A., van Paradijs J., Pedersen H., van der Klis M., 1989, *A&A*, 210, 114
- Claret A., 1998, *A&A*, 335, 647
- Claret A., 2000, *A&A*, 363, 1081
- Collins G. W., II, Truax R. J., 1995, *ApJ*, 439, 860
- Conner J. P., Evans W. D., Belian R. D., 1969, *ApJ*, 157, L157
- Cowley A. P., Hutchings J. B., Schmidtke P. C., Hartwick F. D. A., Crampton D., Thompson I. B., 1988, *AJ*, 95, 1231
- D'Avanzo P., Campana S., Casares J., Israel G. L., Covino S., Charles P. A., Stella L., 2005, *A&A*, 444, 905
- D'Avanzo P., Muñoz-Darias T., Casares J., Martínez-Pais I. G., Campana S., 2006, *A&A*, 460, 257
- Davey S., Smith R. C., 1992, *MNRAS*, 257, 476
- Dhillon V. S., Watson C. A., 2001, in Boffin H. M. J., Steeghs D., Cuypers J., eds, *Lecture Notes in Physics*, Vol. 573, *Astromotography, Indirect Imaging Methods in Observational Astronomy*. Springer-Verlag, Berlin, p. 94
- Donati J.-F., Collier Cameron A., 1997, *MNRAS*, 291, 1
- Donati J.-F., Semel M., Carter B. D., Rees D. E., Collier Cameron A., 1997, *MNRAS*, 291, 658
- Eggleton P. P., 1983, *ApJ*, 268, 368
- Gelino D. M., Harrison T. E., Orosz J. A., 2001, *AJ*, 122, 2668
- González Hernández J. I., Rebolo R., Israelian G., Casares J., Maeda K., Bonifacio P., Molaro P., 2005, *ApJ*, 630, 495
- Gray D. F., 1992, *Compact Stellar X-ray Sources*. Cambridge Univ. Press, Cambridge
- Hauschildt P. H., Allard F., Baron E., 1999, *ApJ*, 512, 377
- Horne K., Wade R. A., Szkody P., 1986, *MNRAS*, 219, 791
- Khargharia J., Froning C. S., Robinson E. L., 2010, *ApJ*, 716, 1105
- Kupka F. G., Ryabchikova T. A., Piskunov N. E., Stempels H. C., Weiss W. W., 2000, *Balt. Astron.*, 9, 590
- Lucy L. B., 1967, *Z. Astrophys.*, 65, 89
- Ma B., Li X.-D., 2009, *ApJ*, 691, 1611
- McClintock J. E., Remillard R. A., 1990, *ApJ*, 350, 386
- Marsh T. R., Horne K., 1988, *MNRAS*, 235, 269
- Marsh T. R., Robinson E. L., Wood J. H., 1994, *MNRAS*, 266, 137
- Matsuoka M. et al., 1980, *ApJ*, 240, L137
- Paczyński B., 1971, *ARA&A*, 9, 183
- Pylyser E., Savonije G. J., 1988, *A&A*, 191, 57
- Rappaport S., Verbunt F., Joss P. C., 1983, *ApJ*, 275, 713
- Robinson E. L., Barker E. S., Cochran A. L., Cochran W. D., Nather R. E., 1981, *ApJ*, 251, 611
- Rutten R. G. M., Dhillon V. S., 1994, *A&A*, 288, 773
- Sarna M. J., 1989, *A&A*, 224, 98
- Schatzman E., 1962, *Ann. Astrophys.*, 25, 18
- Shahbaz T., 1998, *MNRAS*, 298, 153
- Shahbaz T., 2003, *MNRAS*, 339, 1031
- Shahbaz T., Watson C. A., 2007, *A&A*, 474, 969
- Shahbaz T., Naylor T., Charles P. A., 1993, *MNRAS*, 265, 655
- Shahbaz T., Smale A. P., Naylor T., Charles P. A., van Paradijs J., Hassall B. J. M., Callanan P., 1996, *MNRAS*, 282, 1437
- Shahbaz T., Groot P., Phillips S. N., Casares J., Charles P. A., van Paradijs J., 2000, *MNRAS*, 314, 747
- Shahbaz T., Dhillon V. S., Marsh T. R., Casares J., Zurita C., Charles P. A., 2010, *MNRAS*, 403, 2167
- Spruit H. C., Ritter H., 1983, *A&A*, 124, 267
- Tonry J., Davis M., 1979, *AJ*, 84, 1511
- Torres M. A. P., Casares J., Martínez-Pais I. G., Charles P. A., 2002, *MNRAS*, 334, 233
- van der Sluys M. V., Verbunt F., Pols O. R., 2005, *A&A*, 440, 973
- Verbunt F., Zwaan C., 1981, *A&A*, 100, L7
- Watson C. A., 2002, PhD thesis, Univ. Sheffield
- Watson C. A., Dhillon V. S., 2001, *MNRAS*, 326, 67
- Watson C. A., Dhillon V. S., 2004, *Astron. Nachr.*, 325, 189
- Watson C. A., Dhillon V. S., Rutten R. G. M., Schwope A. D., 2003, *MNRAS*, 341, 129
- Watson C. A., Dhillon V. S., Shahbaz T., 2006, *MNRAS*, 368, 637
- Watson C. A., Steeghs D., Shahbaz T., Dhillon V. S., 2007, *MNRAS*, 382, 1105
- Welsh W. F., Horne K., Gomer R., 1995, *MNRAS*, 275, 649
- Zurita C., Casares J., Shahbaz T., 2003, *ApJ*, 582, 369

This paper has been typeset from a $\text{\TeX}/\text{\LaTeX}$ file prepared by the author.